TÜBİTAK

Turkish Journal of Earth Sciences
http://journals.tubitak.gov.tr/earth

Research Article

Turkish J Earth Sci
(2021) 30: 1045-1060

doi: 10.3906/yer-2106-15

Harcourt granite scCO$_2$ water interaction: a laboratory study of reactivity and modelling of hydrogeochemical processes

Badulla Liyanage AVANTHI ISAKA, Ranjith Pathegama GAMAGE*
Department of Civil Engineering, Monash University, Building 60, Melbourne, Victoria, Australia

Received: 17.06.2021 **Accepted/Published Online:** 28.09.2021 **Final Version:** 01.12.2021

Abstract: Batch-type laboratory reactivity experiments and modelling of hydrogeochemical interactions of a granite-scCO$_2$-water system were conducted at 100 °C and 10 MPa in order to evaluate the geochemical and mineralogical responses of the granite to long-term reaction. The laboratory reactivity tests were conducted for a total duration of 70 days, and the continued hydrogeochemical interactions for up to 210 days were determined by geochemical simulations. The reacted granite powder and the residual solutions were subjected to several analytical techniques, including inductively-coupled plasma optical emission spectrometry (ICP-OES), X-ray diffraction (XRD), scanning electron microscopy (SEM) and pH measurements, in order to characterise the mineralogical interactions. The fluid chemistry of the residual solutions shows that significant dissolution occurs in Harcourt granite at the initial stages of saturation. Hence, the Na, K, Ca, Mg, Al, Fe and Si concentrations increase in the solution. The dissolution of anorthite, albite and biotite minerals continues with time, whereas the dissolution of quartz is comparatively slow in the system. However, the Ca, Mg, Al, and Si concentrations gradually decrease with the increase of reaction time due to the formation of secondary precipitants. Metastable clay minerals such as smectite, illite, and kaolinite precipitate in the saturation medium with time. The permanent deposition of clay minerals in the upper boundary of the geothermal reservoir is beneficial for the creation of a sealing zone for geothermal reservoirs. Importantly, calcite precipitation occurs with the long-term saturation of the system, and, hence, there is potential for CO$_2$ trapping in the outer uppermost periphery of CO$_2$-based geothermal reservoirs with long-term operation.

Key words: CO$_2$-based geothermal reservoirs, mineral interactions, Harcourt granite, long-term operation of enhanced geothermal systems (EGSs), PHREEQC model

1. Introduction

The use of CO$_2$ as the working fluid in enhanced geothermal systems (EGS) has recently been considered to be a promising approach to the coupling of geothermal energy extraction with deep geological sequestration of anthropogenic CO$_2$ (Randolph and Saar, 2011; Li et al., 2016; Isaka et al., 2019; Singh et al., 2020; Chandrasekharam et al., 2019; Tugay et al., 2021). In addition, the properties of CO$_2$, including its low viscosity and great expansivity and compressibility with temperature change, indicate the potential use of CO$_2$ as the working fluid in EGS, replacing the traditional water-based method (Brown, 2000).

CO$_2$-based EGS have the potential to sequestrate CO$_2$, either by the loss of injected fluid into the surrounding permeable rock formation in EGS if it is sufficiently permeable or by CO$_2$ trapping through mineral dissolution and precipitation during long-term interaction. The strategy of sequestration of CO$_2$ in a geothermal reservoir is shown in Figure 1 (Ueda et al., 2005). Water, which is present in the inner zone of geothermal reservoirs, either in the gas phase or liquid form, dries out and is displaced over time by the CO$_2$ flume (Ré et al., 2014). The minerals, which were initially dissolved in the pore fluid of the geothermal reservoir, are left behind as secondary mineral precipitants by the CO$_2$ stream (Brown, 2000). However, the reactivity of CO$_2$ with the rock minerals present in the inner dry zone of the reservoir is insignificant over time. CO$_2$ diffused into the outer periphery of the reservoir dissolves in the pore fluid of the surrounding rock formation, increasing the acidity of the pore fluid (Suto et al., 2000). Therefore, the enhanced reactivity of the acidified pore fluid accelerates the mineral-fluid interactions over time. The mineral dissolution and precipitation phenomena result in the alteration of the microstructure of the rock formation and, therefore, the mass transfer properties of the geothermal reservoir, including rock matrix permeability (Xu et al., 2014). Hence, the heat extraction efficiency and productivity of geothermal reservoirs alter with time. Importantly, significant sequestration of CO$_2$ takes place at the outer periphery of the reservoir due to the enhanced reactivity of the acidified pore fluid (Xu, 2012; Na et al., 2015). It has been identified that a sealing layer develops over the outer periphery of the reservoir due to the dominant mineral precipitation in permeable rock formations (refer to Figure 1) (Ueda et al., 2005). This phenomenon prevents the degassing and leaking of the injected CO$_2$ into the overlying rock formations of geothermal reservoirs, ensuring the safe operation of CO$_2$-based geothermal reservoirs coupled with the safe

*Correspondence: ranjith.pg@monash.edu

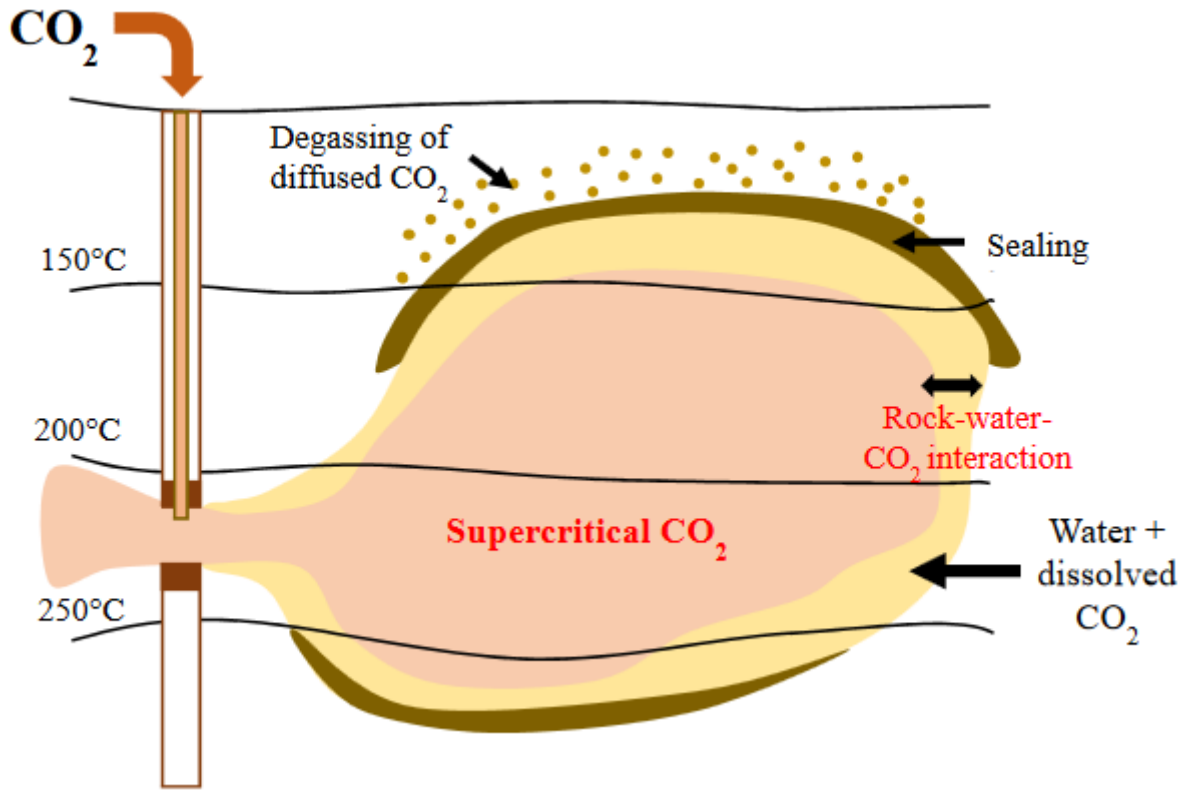

Figure 1. Strategy of CO_2 sequestration in geothermal reservoirs (modified after Ueda et al., 2005).

storage of CO_2 in deep earth during energy extraction from hot dry rocks.

A significant part of research has been carried out recently to investigate the water-rock interactions of CO_2-based geothermal reservoirs. In order to simulate deep geological conditions, researchers have focused on the injection of CO_2 in the supercritical state into their experimental systems, since the critical point is 31.0 °C and 7.38 MPa (Span and Wagner, 1996). Ré et al. (2014) conducted hydrothermal experiments to evaluate the geochemistry and the mineralogical response of granite exposed to water, with and without the presence of supercritical CO_2 (sc CO_2) at 250°C and 25–45 MPa. The study reveals that metastable smectite precipitation takes place in water-saturated granite with the injection of sc CO_2, while the dissolution of minerals such as K-feldspar, oligoclase, and quartz occurs with time. Ré et al. (2014) further concluded that rock carbonation occurred during cooling and degassing in their experiments, and, hence, CO_2 sequestration in geothermal systems requires an extended period of reservoir operation. Suto et al. (2007) conducted batch-type experiments to evaluate the reactivity of granite in a CO_2-saturated system over a wide temperature range of 100 to 350 °C at 25 MPa. This study found that the addition of CO_2 to a hydrothermal system enhances the reactivity of granite with the initial dissolution of minerals (significant dissolution of plagioclase phase) followed by secondary precipitation of clay minerals such as kaolinite, smectite, muscovite, and calcite. Further, the precipitation of aluminium silicates and calcium-aluminosilicates as secondary precipitants confirms the fixation of CO_2 in a hydrothermal system with CO_2 and granite (Liu et al., 2003). In addition, it has been identified that the effect of CO_2 is quite small at 350 °C, and, hence, moderate temperatures of 150–250 °C have been pinpointed as favourable for the capture of CO_2 (Suto et al., 2007). In addition, a study by Ueda et al. (2005) revealed that the calcium from granitic silicates can easily be removed as $CaCO_3$, $CaSO_4$, or CO_2 during CO_2 sequestration in geothermal reservoirs. Moreover, Remoroza et al. (2015) concluded that the increase in the H_2O content of a CO_2-rock hydrothermal system causes increased mineral dissolution and the formation of pits and cavities in granite. However, Jung (2014) revealed that the precipitation of carbonates and clay minerals does not significantly influence the permeability enhancement of geothermal reservoirs in the short term, and this occurs a long period after ceasing the injection of CO_2. However, most researchers (Lin et al., 2008; Xu et al., 2008; Petro, 2013; Pan et al., 2017) have concluded that the injection of CO_2 into a hydrothermal system with granite and water causes the initial hydrolysis of mineral phases followed by the formation of secondary precipitants, which results from both short-term and long-term reactions. Hence, the combination of mineral dissolution and precipitation in the peripheral zone of the geothermal reservoir affects the geological storage of CO_2,

reservoir growth, and the productivity of the geothermal system in the long term.

However, the studies of hydrotherma systems and batch experiments reported in the literature have only considered geochemical reactions for short periods with a maximum period of 28 days (Lo Ré et al., 2012; Ré et al., 2014). Nevertheless, the literature shows that the duration of reaction profoundly impacts the formation of secondary minerals from the ions released to the geofluid after initial mineral dissolution. Furthermore, the equilibrium conditions of the possible reactions of granite with sc CO_2-dissolved water were not achieved in the experiments reported in the literature (Remoroza et al., 2015). Hence, it is vital to evaluate the reactivity of granite exposed to water with sc CO_2 in order to have a clear understanding of the long-term geochemistry of a CO_2-based geothermal reservoir under continuous operation. Therefore, the aim of the present study is to investigate the long-term mineralogical interactions and geochemistry of a granite-sc CO_2-water system by conducting a batch reactivity experiment at 100 °C and 10 MPa. The temperature of 100 °C was selected for the batch experiment, since CO_2 capture is encouraged in geothermal reservoirs with moderate temperatures (Suto et al., 2007). Water-rock interactions were evaluated for a total period of 10 weeks, and geochemical modelling was conducted based on the reaction kinetics obtained from the experimental results, and modelling continued for a period of 20 weeks in order to evaluate the long-term mineralogical interactions.

2. Experimental methodology

2.1. Harcourt granite used for reactivity analysis

Harcourt granite sourced from Mount Alexander, Victoria, was selected as the test material for the reactivity investigations included in the study. The results of X-ray diffraction (XRD) tests reveal that Harcourt granite is mainly composed of quartz, biotite, plagioclase, and K-feldspar. The mineralogical composition and petrophysical properties of Harcourt granite are shown in Table 1. Ground granite with particle sizes ranging from 150 to 350 μm was used for the reactivity tests, and the particle size distribution of the powder in the range of 150–350 μm is shown in Figure 2. The effective particle diameter was determined to be 248 μm.

Powdered granite was rinsed with distilled water and oven-dried at 80 °C for 48 h in order to remove dust and moisture prior to testing. A SEM image of granite powder prepared for the tests is shown in Figure 3 with the energy-dispersive spectroscopy (EDS) analysis. An abundance of elements such as Si, Al, Na, Mg, and Ca was found, based on the EDS analysis of the granite used in the tests.

2.2. Experimental set-up for batch reactions

A mixture of rock and distilled water with a water/rock ratio of 1:10 was poured into the reaction vessel of the reaction chamber used for the tests of rock-water interactions. The high-temperature and high-pressure

Table 1. Petrophysical properties of Harcourt granite.

Mineralogy: Quartz (SiO_2) Biotite ($K(Mg,Fe)_3AlSi_3O_{10}(OH)_2$) Plagioclase (Albite dominated) ($NaAlSi_3O_8$ – $CaAl_2Si_2O_8$) K-feldspar ($KAlSi_3O_8$)	Percentage by mass: 31.3% 6.7% 33.8% 28.1%
Density	2.68 g/cm^3
Effective diameter	248 μm
Geometric surface area	9.03 m^2/kg

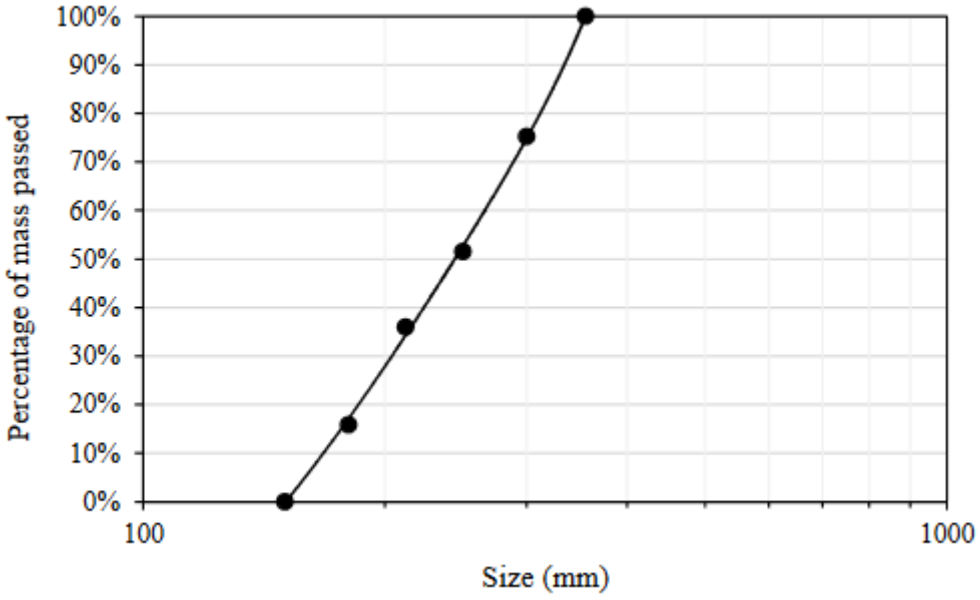

Figure 2. Particle size distribution of Harcourt granite powder ranging from 150 to 350 μm.

reaction chamber used in the study is shown in Figure 4, highlighting the fluid injection paths and pressure control devices. Once the mixture of granite and water was placed in the reaction vessel, the chamber was carefully sealed using an 'O' ring and steel bolts in order to avoid fluid leakage. The reaction vessel and injection tubing are made of stainless steel in order to avoid corrosion and reaction of the acidic medium with the chamber.

Initially, the reaction chamber was pressurised up to 10 MPa using a syringe pump with 99.9% CO_2 pumped from the gas cylinder. The CO_2 pressure in the reaction vessel was monitored by a pressure gauge fixed to the injection lines. The system was allowed to stabilise the pressure for 24 h before the initiation of heating. Once the pressure was stabilised, the chamber was heated to 100 °C by covering the reaction vessel with a heating band. The temperature and pressure values of the reactivity study were maintained in order to represent the geological conditions of the upper-most layers of CO_2-based geothermal reservoirs. CO_2 at 100 °C and 10 MPa behaves

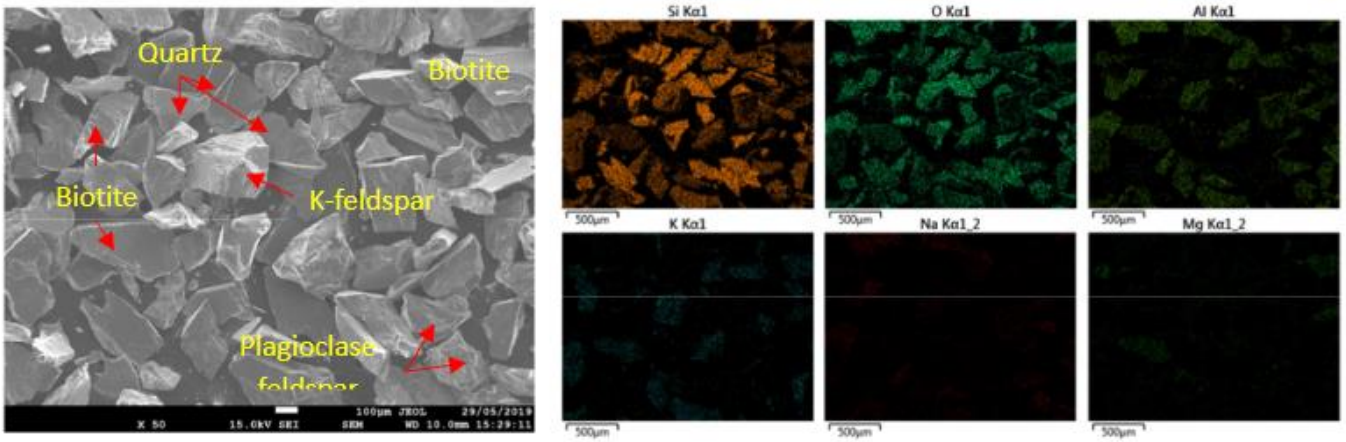

Figure 3. SEM image and EDS analysis of powdered granite used for reactivity tests.

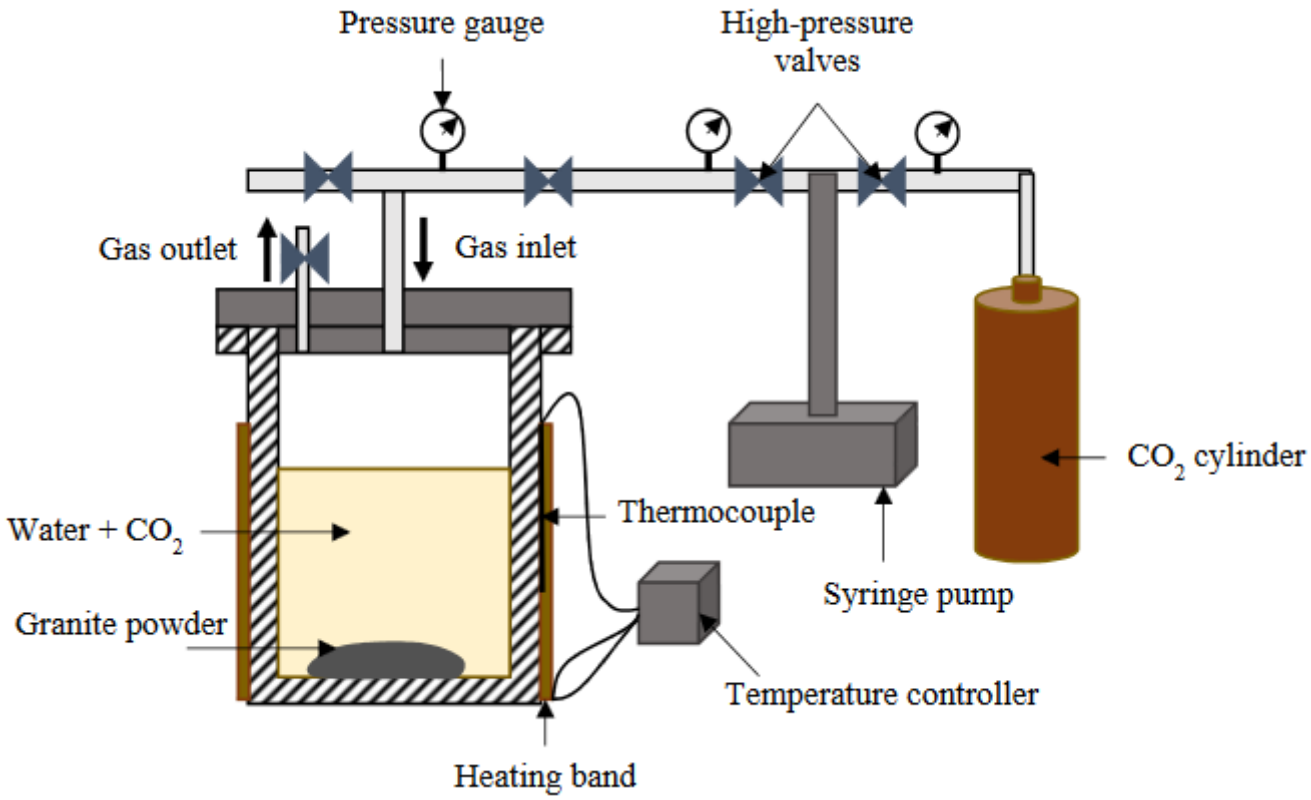

Figure 4. High-pressure reaction chamber used in study of granite/water/CO_2 interactions.

as a supercritical fluid (sc CO_2) with 1.4% molar solubility in water, since its critical point is 31.10 °C and 7.39 MPa (Suto et al., 2000). The temperature of the chamber was controlled using a thermocouple fixed to the vessel (refer to Figure 4). The increase of pressure in the vessel due to the expansion of gas-phase CO_2 was controlled by the syringe pump, so that constant pressure of 10 MPa was maintained in the reaction vessel. During the experiments, the rock powder was maintained in suspension by stirring the solution uniformly at a constant speed. The system was kept closed in order to provide space for water-rock interactions to take place over time. Both liquid and powdered samples were removed from the chamber at different time periods of 2 days, 4 days, 7 days, 14 days. 21 days, 42 days, 63 days, and 70 days for the conduct of analytical tests. The pressure in the reaction chamber was released, and the system was cooled before the samples were removed from the vessel. This method was followed since no drainage valve is connected to the chamber, which is an experimental limitation. The system was sealed immediately after the samples were taken, and pressurised and heated immediately after removing the samples. The liquid solutions were immediately used for ICP-OES analysis, while the powdered samples were directed to XRD analysis and SEM imaging.

2.3. Analytical methods adopted

2.3.1. Scanning electron microscopy (SEM) analyses of reacted granite powder

The reacted granite removed from the reaction chamber was drained using a filter paper and oven-heated at 80 °C for 24 h to remove the moisture from the sample. The powder was then immediately sent for SEM analyses. The JOEL 7001F microscope available at the Monash Centre for Electron Microscopy (MCEM) was used for SEM imaging throughout the study (refer to Figure 5(a)). Specimens prepared for SEM analyses were coated with carbon in order to avoid the charging effect and over-illumination of the images. SEM imaging and energy dispersive spectroscopy (EDS) analyses were carried out following the standard EDS process with an accelerating voltage of 15kV, 10 mm working distance, and a probe current of 10. EDS analyses was conducted of selected areas of each specimen to identify the mineral composition of the new precipitants and to identify the mineralogy of pitted areas.

2.3.2. X-ray diffraction analyses

Powder XRD analyses were conducted on granite powder reacted for different time durations using the D8 cobalt XRD instrument shown in Figure 5(b). The XRD recordings were taken using Kα radiation of Cu at 40.0 kV and 25.0 mA for a 2θ range of 5 to 90. Semiquantitative analyses, based on the integrated areas of the peaks of corresponding mineral phases, were adopted to determine the mineralogical composition of the reacted granite powder. DIFFRAC EVA software (4.3 version) was used for the semiquantitative analyses of the results. XRD analyses were conducted only on selected sampling stages, since the loss of material would affect the experiment. Therefore, XRD analysis was conducted for granite powder reacted for 7 days, 14 days, 21 days, 42 days, and 70 days.

2.3.3. Inductively-coupled plasma optical emission spectroscopy (ICP-OES) analyses

The liquid samples removed from the chamber were subjected to ICP-OES analysis at the PerkinElmer Flagship testing facility (shown in Figure 5(c)) at the Monash Analytical Platform in order to determine the fluid chemistry of the samples. The liquid solutions were filtered using 0.45 µm filter paper to remove solids suspended in the solutions, and the filtrate was diluted two times using 1% HNO_3. The solutions were acidified to avoid the precipitation and clogging of dissolved metals (Pereira et al., 2011). The concentrations of dissolved metals in the solutions were determined by following the corresponding calibration charts, which were separately developed for different elements. The pH values of these solutions were also measured using a pH meter 1 h after the solutions reached atmospheric temperature and pressure.

2.4. Geochemical modelling

2.4.1. Determination of saturation indices (*SI*)

Geochemical modelling of the granite-water- CO_2 interactions was carried out using PHREEQC software (3.4.0 version) based on the LLNL.dat database (Parkhurst, 1995). Calculations of reactive kinetics and equilibrium speciation concentrations were based on the measured compositions of the final solutions. The saturation indices (*SI*) of different mineral phases in the solution, which depend upon the elemental concentrations in the liquid samples, were calculated at different time intervals. The calculation of *SI* is based on Eq. 1 where, *IAP* is the ion activation product and the K_{SP} is the solubility product of the corresponding mineral phase (Boudot et al., 1996). Positive values for *SI* indicate that the minerals are likely to precipitate, whereas negative values for *SI* show the dissolution of mineral phases.

$$SI = log\ (\frac{IAP}{K_{sp}}) \quad (1)$$

2.4.2. Calculation of the initial pH value of solutions

Aqueous CO_2 is characterised as H_2CO_3, and the initial pH value of a solution with dissolved CO_2 is determined with reference to the dissociation of H_2CO_3 into H+ and H_2CO_3 , as shown in Eq. 2. The equilibrium constant (K) for the reaction is defined using Eq. 3, where $[H^+]$ and $[HCO_3]$ stand for the activities of H^+ and HCO_3 , respectively and f_{CO2} is the fugacity of CO_2 gas at a given temperature and pressure. Here, the f_{CO2} is assumed to be the partial pressure of CO_2 at 100 °C and 10 MPa (Suto et al., 2007). According to the charge balance, $[H^+] = [HCO_3]$ under initial conditions, and, hence, the initial pH value can be determined using Eq. 4. The calculated initial pH value of the solution at 100 °C and 10 MPa was 3.68.

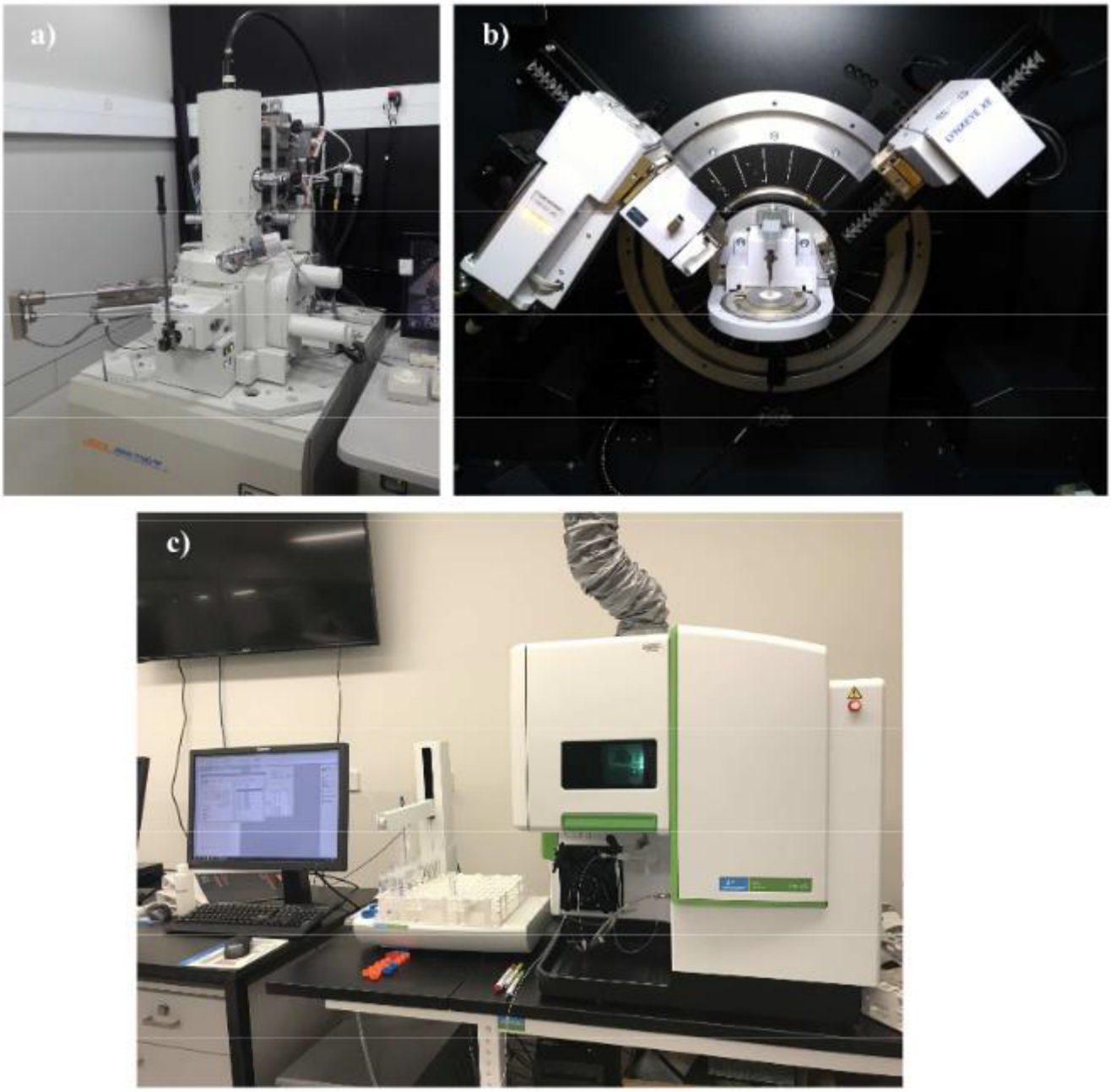

Figure 5. (a) JOEL 7001F microscope available at MCEM, (b) D8 Cobalt XRD instrument and (c) ICP-OES set-up available at Monash Analytical Platform.

$$CO_2\ g\ + H_2O = H^+ + HCO_3^- \quad (2)$$

$$\log K\ = log\ H^+\ + \log HCO_3^-\ - log f_{CO_2} \quad (3)$$

$$2pH = -\log(K) - log f_{CO_2} \quad (4)$$

2.4.3. Determination of reaction rates and composition of equilibrium phases

Batch geochemical modelling was performed to predict the mineral compositions of Harcourt granite at different time durations during granite-water- CO_2 interactions. The dissolution and precipitation of different mineral phases were determined based on the initial mineralogy of granite, CO_2 solubility under corresponding temperature and pressure conditions, the composition of the initial liquid solution, and the kinetic rates of mineral phases (Jayasekara et al., 2020). The total pressure of 10 MPa at 100 °C was equilibrated with the initial solution with different mineral phases. It should be noted that the partial pressure of CO_2, which is the difference between the total pressure and the water vapour pressure at 100 °C, was set at 9.99 MPa (Alemu et al., 2011). Accordingly, the simulation was run for a duration of 30 weeks. The amounts of different mineral phases in the initial solution per kg of water were determined on the basis of the water/rock ratio. In addition, it was assumed that the contribution of CO_2 in the rock-mineral interaction is to increase the acidity level of the solution

with the supply of photons. Hence, there is no direct effect on the dissolution of silicate materials in the solution (Golubev et al., 2005; Hänchen et al., 2006). Alemu et al. (2011) further explained that the influence of dissolved CO_2 on carbonate precipitation is insignificant compared to its influence on increasing the acidity level of the solution. Therefore, the general form of the rate law given in Eq. 5 developed from the transition state theory (Aagaard and Helgeson, 1982; Lasaga, 1984; Alemu et al., 2011) was incorporated to calculate the kinetic rates of acidity-driven dissolution and precipitation reactions.

In Eq. 5, $Rate_m$ is the dissolution or precipitation of m mineral phase, and positive values denote dissolution, and negative values denote precipitation of the corresponding mineral phase. A is the reactive surface area per one kilogram of water, $k(T)$ is the reaction rate constant for the considered temperature, a_{HT} is the photon activity, n is the order of the reaction, K is the equilibrium constant of the considered reaction, and Q is the ion activity product. The temperature-dependent reaction rates were also calculated with reference to the reaction rates at 25 °C based on Arrhenius' law (Laidler, 1972; Aquilanti et al., 2010), given in Eq. 6. In Eq. 6, k_{25} is the reaction rate at 25 °C for the considered reaction in $molm^{-2}s^{-1}$, E_a is the activation energy in $Jmol^{-1}$, R is the gas constant, which is 8.314 J $mol^{-1}K^{-1}$, and T is the temperature in Kelvin. The reaction rate constants for mineral phases were obtained from previous studies, and the calculated values at 100 °C based on Eq. 6 are given in Table 2 with the corresponding reference study. Other parameters used for the simulation are also included in Table 2. In the calculation of the surface areas of mineral grains, a spherical shape with an effective diameter was considered for all mineral phases. It should be noted that all the minerals were allowed to dissolve and precipitate, and similar reaction rates were used for both dissolution and precipitation processes (Alemu et al., 2011). Plagioclase phase feldspar was introduced to the model as 75% albite and 25% anorthite, and biotite was introduced as 44% annite and 56% phlogopite. The surface area of the clay minerals was calculated by assuming spherical grains of 2 μm (Alemu et al., 2011).

$$Rate_m = A_m k(T)_m (a_{H+}^n)\left(1 - \left(\frac{Q_m}{K_m}\right)\right) \quad (5)$$

$$k(T) = k_{25} \exp\left(\frac{-E_a}{R}\right)\left(\frac{1}{T} - \frac{1}{298.15}\right) \quad (6)$$

3. Results and discussion

3.1. Dissolution of primary minerals in Harcourt granite

3.1.1. Experimental findings from fluid chemistry and SEM imaging

A qualitative understanding of the dissolution of different minerals of Harcourt granite was obtained by analysing the fluid chemistry and SEM images. The variations of different elemental concentrations of the liquid solutions with the increase of reaction time are shown in Figure 6. The increase in concentrations of elements such as Si, Fe, Al, Ca, Mg, Na, and K, which were absent in the initial solution, characterises the initial dissolution of Harcourt granite in the presence of CO_2-dissolved water at 100 °C and 10 MPa. Concentrations of Si, Na, K, and Ca ions in the solution are comparatively higher than the Al, Fe, and Mg ion concentrations. As Figure 6 shows, the concentrations of almost all the elements increase with the increase of reaction duration up to 14 days, whereas the Na^+ and K^+ ion concentrations increase continuously with a further increase in time. The release of Na^+ and K^+ ions into the solution characterises the dissolution of K-feldspar and albite minerals. However, the origin of K^+ ions in the solution cannot be distinguished between K-feldspar and biotite. Furthermore, the Si ion concentration peaked at 74 ppm after 7 days and reduced by 52% of the peak value with the increase of reaction duration up to 70 days. Similarly, the Al^{3+} concentration peaked at 7 days and

Table 2. Parameters used in geochemical modelling.

Mineral	Mass (mol/kg of water)	Surface area (m^2/g)	E_a (kJ/mol)	n	log (k_{25}) ($molm^{-2}s^{-1}$)	log (k_{100}) ($molm^{-2}s^{-1}$)	Reference
Quartz	0.521	0.0091	90.90	0.00	−13.41	−-10.21	Palandri and Kharaka (2004)
K-feldspar	0.101	0.0095	51.70	0.50	−10.06	−8.24	Palandri and Kharaka (2004)
Anorthite	0.030	0.0086	16.60	1.41	−8.00	−7.42	Palandri and Kharaka (2004)
Albite	0.096	0.0092	65.00	0.50	−12.00	−9.71	Palandri and Kharaka (2004)
Annite	0.006	0.0072	22.00	0.37	−11.85	−11.08	(Xu et al., 2011)
Phlogopite	0.011	0.0085	66.90	0.40	−10.47	−8.11	(Krausz, 1974; Kalinowski and Schweda, 1996)
Illite	0	0.0088	46.00	0.10	−12.40	−10.78	(Köhler et al., 2003)
Smectite-high-Fe-Mg	0	0.0105	23.60	0.50	−10.98	−10.15	(Palandri and Kharaka, 2004)
Calcite	0	0.0089	14.40	0.50	−0.30	0.21	(Palandri and Kharaka, 2004)
Kaolinite	0	0.0100	65.90	0.20	−11.30	-8.99	(Palandri and Kharaka, 2004)

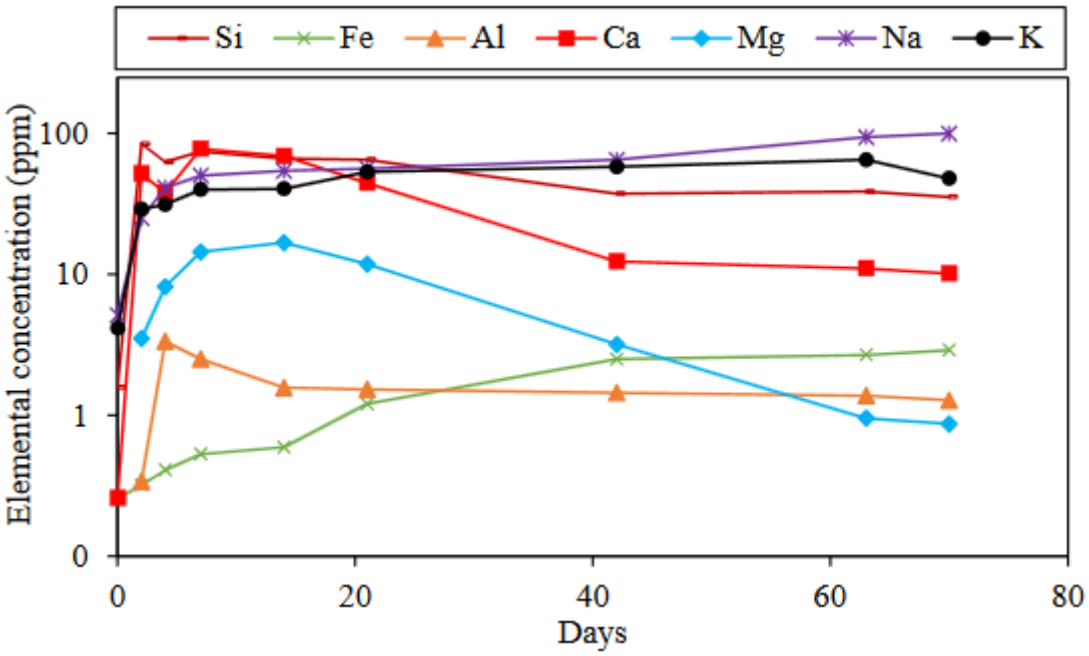

Figure 6. Variations of elemental concentrations of liquid samples determined by ICP-OES tests.

appeared to decrease with a further increase in reaction time. The continuous increase in Fe ion concentration indicates the dissolution of biotite mineral with time, since the only source of Fe is biotite. The Ca and Mg ion concentrations followed the consistent behaviour of an initial increase followed by gradual reductions in concentrations with time. The reductions of Al, Ca, Mg, Fe, and Si ion concentrations are due to the formation of secondary precipitants (clay minerals, aluminosilicates, and other transitional products of Fe) when the solution is over-saturated with these minerals.

The measured pH values during sampling were in the range of 3.81–5.02 and slightly increased with the increase of reaction time due to the consumption of H^+ ions for the reactions of mineral dissolution and precipitation. SEM images of the reacted granite powder further explain the dissolution phenomenon of K-feldspar, quartz, anorthite, and biotite minerals in Harcourt granite. Pitting textures were observed in K-feldspar and quartz mineral grains at initial stages of reaction after 7 days and 21 days, as shown in Figure 7(a) and Figure 7(c), respectively. The dissolution of anorthite and biotite phases was also observed at later stages of reaction after 42 days and 70 days, as shown in Figure 7(b) and Figure 7(d), respectively.

3.1.2. Results of geochemical modelling

Geochemical modelling was conducted to evaluate the geochemistry of the saturated fluid with a further increase of time up to 210 days. A comparison of the simulation results with the results obtained from ICP-OES analysis is shown in Figure 8. In this figure, experimentally-obtained results are plotted as points, whereas simulation results are plotted in lines. The results obtained from the geochemical simulations are consistent with the experiments, with the exception of slight deviations in Fe and Al ion concentrations. These slight variations were possibly due to the changes in kinetic constants in the simulations and inaccuracy in the dilution of the solutions. The SIs calculated for different minerals which were incorporated in the geochemical modelling are recorded in Table 3. Negative values for SIs indicate that the solution is under-saturated with the corresponding ions, whereas positive values indicate that the solution is super-saturated with the corresponding ions with the possibility of mineral precipitation. The release of Ca and Na ions into the solution characterises the initial dissolution of granite in an aqueous medium (Bischoff and Rosenbauer, 1996). In the initial stages, the SIs of anorthite, albite, and K-feldspar are higher than those of quartz, phlogopite, and annite, which were present in the initial granite powder. Therefore, the dissolution of anorthite, albite, and K-feldspar is significant in the initial period of saturation. Furthermore, the rate of dissolution of anorthite (3.84×10^{-8} mol/m^2/s at 100C and pH = 4) is greater than that of other minerals in the solution. The dissolution rates of albite, K-feldspar and quartz are approximately 1.95×10^{-10} mol/m^2/s, 5.76×10^{-9} mol/m^2/s and 6.18×10^{-11} mol/m^2/s (at 100°C and pH = 4) (Palandri and Kharaka, 2004). Hence, anorthite tends to dissolve more quickly in an acidic solution than other minerals, whereas the dissolution of quartz is slow. However, Amrhein and Suarez (1992) found that the addition of Al to the acidic solution slows the dissolution rate of quartz, while there is no effect of Ca and Si ions on the dissolution rate of anorthite. Therefore, the dissolution rate of anorthite varies greatly during the reaction period compared to the initial condition. In all alkali feldspars, Al is more readily hydrolysed from the aluminosilicate framework than Si, since the removal of Al leaves the partially-linked Si-O tetrahedra, and, hence, the

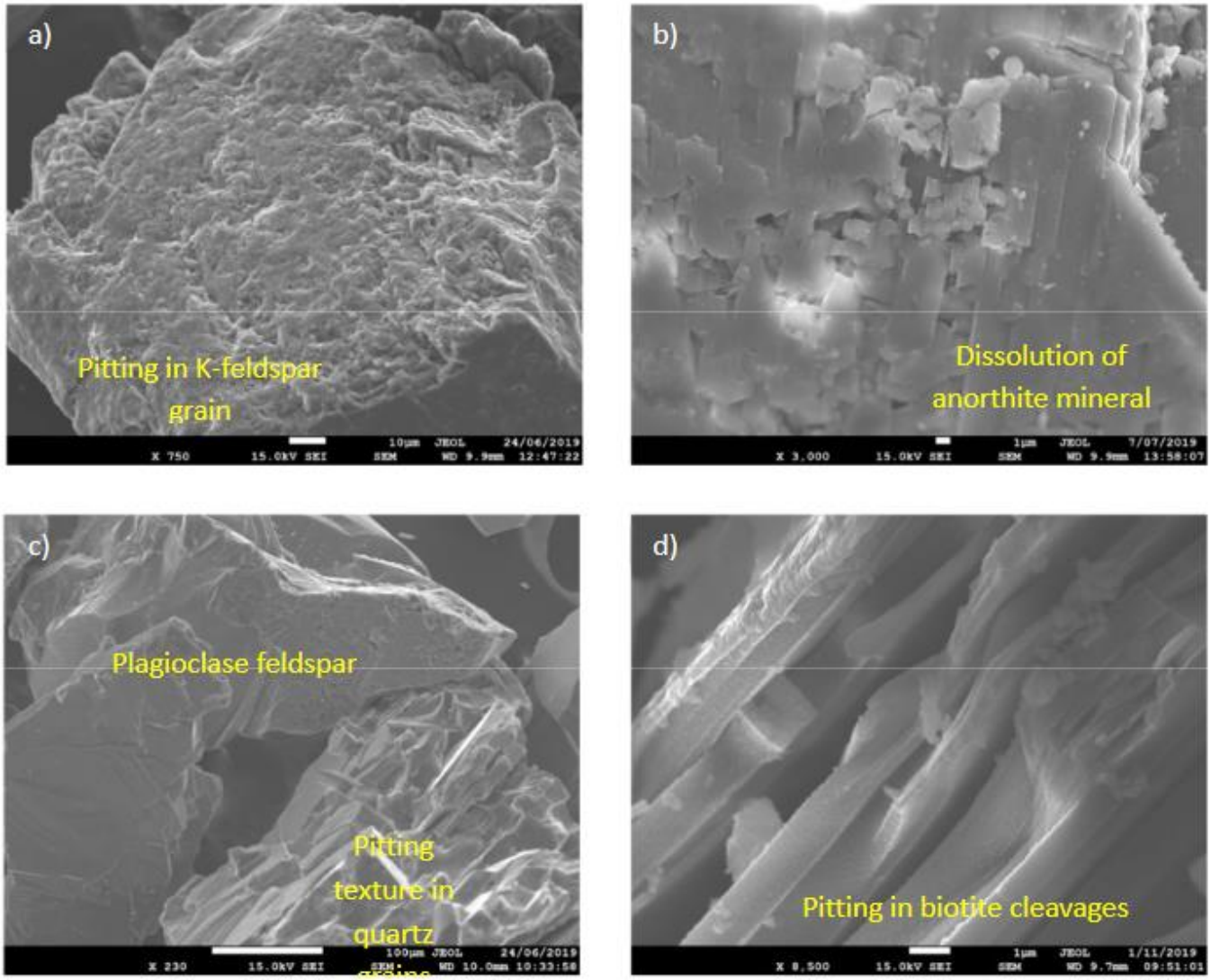

Figure 7. Dissolution and pitting textures observed in SEM images of (a) K-feldspar surface after 7-day reaction, (b) anorthite surface after 42-day reaction, (c) quartz surface after 21-day saturation, and (d) biotite cleavages after 70-day reaction

removal of Si requires the breaking of the Si-O bonds of the tetrahedra (Oelkers and Schott, 1995). Although the rate of dissolution of anorthite reduces with the duration of the reaction, the solution is under-saturated with respect to anorthite even at the end of the simulation period, since it exhibits a SI of –2.02 after 210 days of saturation. Hence, it is evident that anorthite continues to dissolve in the water/CO_2 medium by releasing Si, Ca, and Al ions into the solution as per Eq. 7 (Shvartsev, 2013). However, the SIs for anorthite obtained from simulation results become less negative with the increase of saturation duration (see Table 3).

Similarly, the dissolution of albite and biotite minerals continues up to the end of the simulation period by releasing mainly Si and Al ions to the solution as per Eq. 8 and Eq. 9 (Sugama et al., 2010; Sugama et al., 2011; Gruber et al., 2016). The biotite mineral phase was introduced to the geochemical model as a mixture of phlogopite and annite, and both phases exhibit negative SIs (see Table 3) until the end of the reaction period. Therefore, Mg and Fe ions are continuously released into the solution from the dissolution of the biotite phase. Although albite dissolution is slower than anorthite dissolution, it is faster than that of quartz. Therefore, the initial increase in Si concentration of the solution is mainly due to the hydrolysis of anorthite, albite, and K-feldspar minerals, and the impact of quartz dissolution is insignificant. Further, quartz dissolution takes place according to the generalised Eq. 10 in an aqueous solution, whereas there is no direct impact from dissolved CO_2 on the dissolution reaction, other than an increase in acidity level (Liu et al., 2003; Suto et al., 2007; Lin et al., 2008). Dissolution of K-feldspar releases K, Na, and Al ions into the solution according to Eq. 11 (Kampman et al., 2009), whereas the results of geochemical modelling indicate that K-feldspar dissolution continues with time, except at the end stage of the simulation.

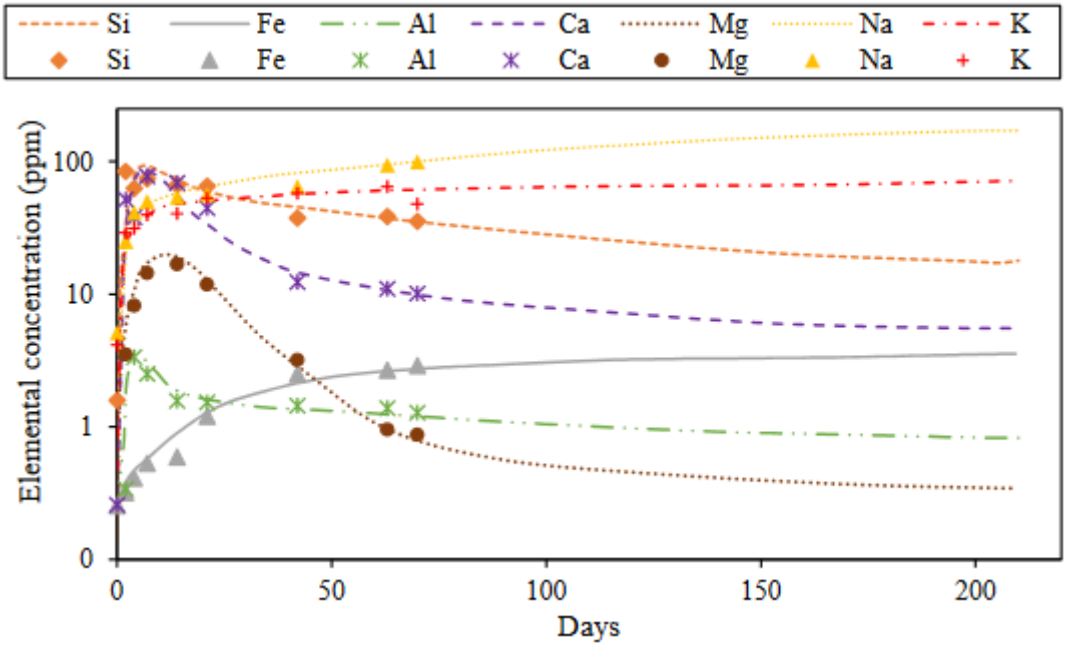

Figure 8. Extended variations of elemental concentrations in liquid samples obtained from geochemical modelling

Table 3. Saturation indices (SIs) of mineral phases calculated using PHREEQC at different time intervals.

	1 week	2 weeks	4 weeks	8 weeks	16 weeks	30 weeks
Quartz; SiO_2	–0.74	–0.27	–0.09	–0.02	0.01	0.06
K-feldspar; $KAlSi_3O_8$	–4.31	–2.84	–1.56	–0.97	–0.24	–0.15
Anorthite; $CaAl_2Si_2O_8$	–6.74	–4.51	–3.58	–2.91	–2.53	–2.02
Albite $NaAl_2Si_3O_8$	–5.71	–4.32	–3.56	–3.04	–2.87	–2.64
Annite $KFe_3^{2+}AlSi_3O_{10}(OH)_2$	–3.95	–2.86	–2.02	–1.83	–1.75	–1.69
Phlogopite $KMg_3AlSi_3O_{10}(F, OH)_2$	–2.87	–1.58	–1.34	–1.25	–1.09	–1.02
Illite $(K,H_3O)(Al,Mg,Fe)_2\ (Si,Al)_4O_{10}\ [(OH)_2,H_2O)]$	0.26	2.67	3.86	4.02	4.54	4.63
Smectite-high-Fe-Mg $(Mg,Fe,Al)_6\ (Si,Al)_4O_{10}\ (OH)_8$	3.65	3.24	3.08	2.96	2.84	2.72
Calcite $CaCO_3$	–3.63	–1.02	–0.08	0.03	0.12	0.19
Kaolinite $Al_2Si_2O_5(OH)_4$	2.21	3.56	4.02	4.35	4.41	4.53

$$CaAl_2Si_2O_8 + 3H_2O + 2CO_2 \leftrightarrow Ca^{2+} + 2Al_2Si_2O_5(OH)_4 + 2HCO_3^- \quad (7)$$

$$NaAlSi_3O_8 + 4H^+ \leftrightarrow AL^{3+} + Na^+ + 3SiO_2 + H_2O \quad (8)$$

$$K(Fe,Mg)_3AlSi_3O_{10}(F,OH)_2 + 12H^+ \leftrightarrow KAlSiO_4 + 2SiO_2 + 3Mg^{2+} + 3Fe^{2+} + 2HF + 2OH^- + 10H^+ \quad (9)$$

$$SiO_2(s) + H_2O \rightarrow SiO_2.nH_2O(aq) \quad (10)$$

$$KNaAlSi_3O_8 + 6H_2O + 2H^+ \leftrightarrow K^+ + Na^+ + Al(OH)_2^+ + 3H_4SiO_4 \quad (11)$$

3.2. Precipitation of secondary minerals

The fluid chemistry of the solutions taken at different reaction durations shows that the ion concentration in the solution peaks at a particular time followed by gradual reductions. In particular, significant reductions in Al, Si, Mg, and Fe ions were observed in the results of both experiments and geochemical modelling, as shown in Figure 6 and Figure 8, respectively. In addition, the calculated SIs for different mineral phases (see Table 3) show that clay minerals such as kaolinite, illite, and

smectite form secondary precipitants with time by consuming ions from the solution.

Hydrolysis of anorthite and albite minerals in an acidic medium results in kaolinization, as given in Eq. 1 and Eq. 2. Hence, kaolinite precipitation can be observed in the early stages of the reaction period, since the dissolution of anorthite and albite is faster. Interestingly, secondary precipitants rich in Al, Si, and O, which may possibly be kaolinite, were observed on top of the plagioclase phase feldspar in Harcourt granite powder reacted for 7 days and 14 days, as shown in Figure 9(a) and Figure 9(b), respectively. These kaolinite precipitants can be characterised as randomly-oriented fine flocculent platelets (Lin et al., 2008). Furthermore, the appearance of new peaks corresponding to kaolinite in the XRD analysis (as shown in Figure 10(a)) further confirms the kaolinization of minerals of granite during reactivity in an acidic medium. Previous studies by Ueda et al. (2001) have shown that the kaolinization of anorthite proceeds at temperatures from 100°C to 250°C, and the reaction rate increases with the increase of acidity level of the medium (Gales, 1905). In addition, continuous hydrolysis of anorthite releases Ca ions into the saturation medium, and the reaction given in Eq. 1 proceeds to the right at high temperatures. Hence, the solution becomes over-saturated with Ca ions with time, and Ca ions are removed from the solution as Ca-silicate minerals or calcite (Ueda et al., 2005). Calcite formation and dissolution take place as per the reaction given in Eq. 6. In the initial stages of the reaction period, the release of Ca^{2+} to the acidic medium by the accelerated hydrolysis of anorthite moves the equilibrium of the reaction towards the right side. However, the increase in CO_2 pressure increases the acidity level of the residual solution, hence contributing to the dissolution of calcite in the acidic solution. Likewise, competing reactions of calcite dissolution and precipitation occur in CO_2-dissolved acidic media. Hence, Hitchon et al. (1999) argued that the continuous formation of calcite cannot be expected in water/granite/CO_2 systems under low pH values.

$$2Ca^{2+} + CO_2(g) + H_2O \leftrightarrow CaCO_3(s) + 2H^+ \quad (12)$$

However, Lin et al. (2008) explained that calcite can be precipitated in a $scCO_2$/vapour/granite system at 100 °C and 10 MPa. According to Lin et al. (2008), only a small amount of water in the form of vapour can be diffused into the $scCO_2$ fluid, and a thin film of water is created on the surface of granite which has the low solubility of $scCO_2$. Since the water in the form of vapour exhibits greater reactivity, the solubility of minerals is accelerated. Hence, there is a possibility of a greater concentration of cations being present in the thin film of water due to the enhanced dissolution of minerals. This phenomenon encourages the forward reaction given in Eq. 12 by forming calcite precipitants in the $scCO_2$/water/granite medium. It is also evident from the results of geochemical modelling that the Mg and Fe concentrations in the residual solution are significantly lower than the Ca concentration, even at the end of the reaction period. Hence, calcite precipitation should occur instead of $MgCO_3$ according to their order of solubility constants ($MgCO_3$> $CaCO_3$> $FeCO_3$) (Lide, 2004). Similar observations were made in the present study. The results for SIs obtained from geochemical modelling for calcite reveal that the fluid medium ($scCO_2$/ vapour/ granite at 10 MPa and 100 °C) is slightly over-saturated with respect to calcite after four weeks of saturation. In addition, precipitants rich in Ca and O (possibly calcite) were observed on the surface of K-feldspar in the SEM images of granite powder reacted for 6 weeks, as shown in Figure 9(c). However, calcite peaks were not observed in the XRD analysis, possibly because the calcite precipitants appeared in very small amounts, which were not available in the powder sample taken for XRD analysis.

Moreover, precipitants rich in Mg, Na, Si, Al, O and K, Mg, Fe, Al, Si, O were observed on quartz surfaces and between biotite cleavages, as shown in Figure 9(d), and Figure 9(e), respectively. These clay mineral precipitants can be characterised as illite, smectite, or a mixture of both. In a previous study by Ré et al. (2014), smectite precipitants were characterised as rosette-forming aluminosilicates, and similar observations were made in the present study. In addition, Ré et al. (2014) interpreted illite as petal-forming structures rich in Mg and Fe. However, the structure of the precipitant observed in the present study (possibly illite) is not clearly visible in the SEM images. Furthermore, smectite and mixed layers of smectite and illite may precipitate in $scCO_2$/water/granite systems at temperatures up to 180 °C and 220 °C, respectively (Henley and Ellis, 1983). Interestingly, clay mineral precipitants were observed in the XRD analysis, and new peaks were observed in the XRD plots of reacted granite in the two-theta range of 5-8°, as shown in Figure 10(b). The presence of a mixture of clay minerals precipitants was also observed close to the two-theta value of 5° in granite reacted for 21 days, 42 days, and 70 days, as highlighted in Figure 10(b). The XRD results for clay mineral precipitants are consistent with those reported in previous studies (Kim et al., 2016; Chen et al., 2020). However, peaks for illite and smectite were not observed in the XRD plots of granite powder reacted for 14 days (see Figure 10(b) and Figure 10(c)), possibly due to a scanning error, since all other XRD plots exhibit the relevant peaks for clay minerals, which can be interpreted as illite and smectite. Moreover, illite precipitation was traced from the peaks of the XRD plots, as shown in Figure 10(c). Precipitation of these clay minerals consumes the cations in the solution such as Mg, Na, K, and Fe, encouraging the dissolution reactions of the mineral phases. In addition, the SIs of illite, smectite and kaolinite are positive, and increase with the increase of reaction time. Hence, the precipitation of these clay minerals takes place throughout the reaction period of 210 days in a $scCO_2$/water/granite system until equilibrium states are reached. In the final stage of the experimental reactivity tests (after 70 days), precipitants of K-aluminosilicates

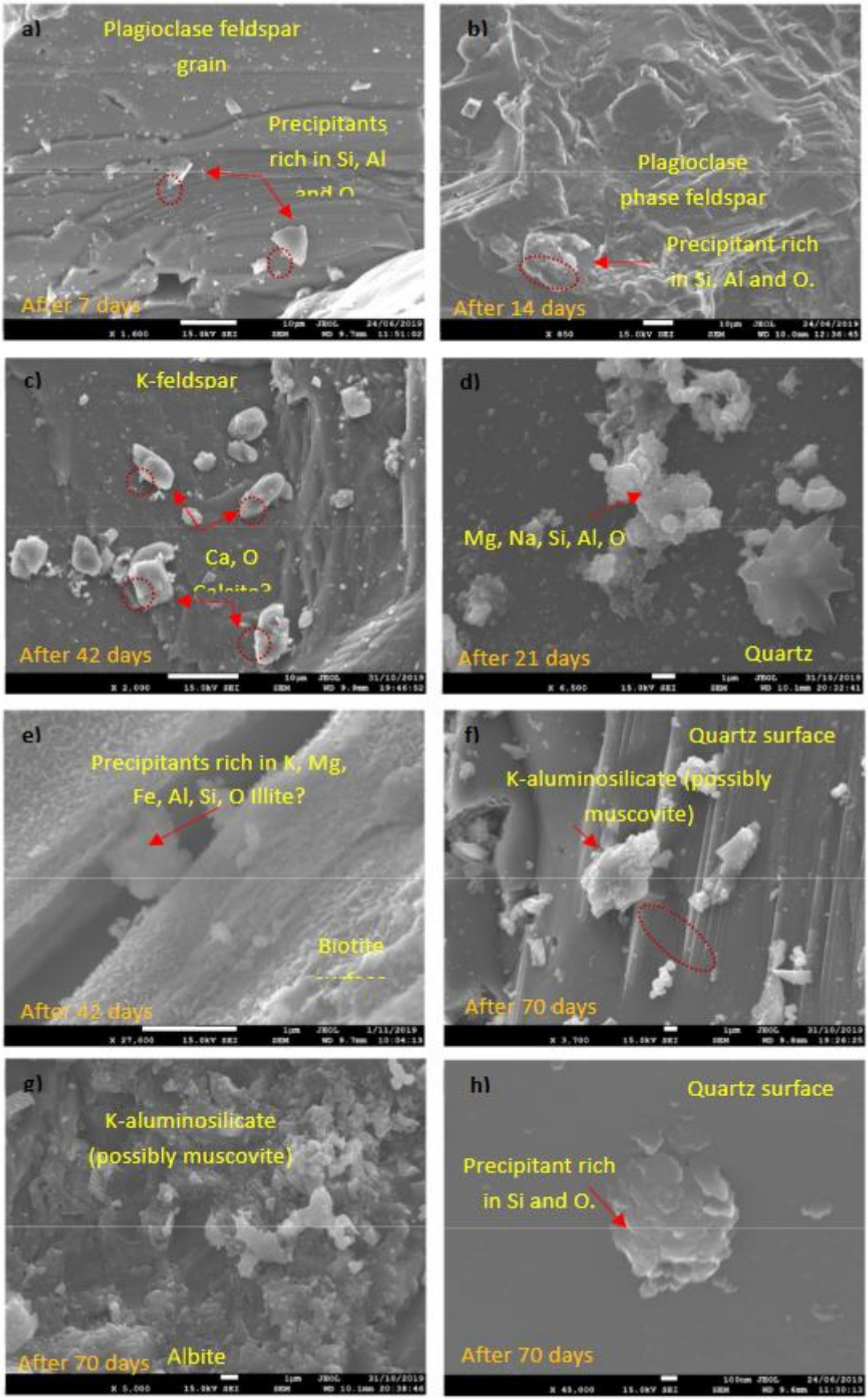

Figure 9. SEM images of newly-formed secondary precipitants at different reaction durations.

were observed, as shown in the SEM images in Figure 9(f) and Figure 9(g). These flaky-like precipitants rich in K, Al and Si elements which appear at high temperatures (300°C) were interpreted as muscovite by Suto et al. (2007). However, it was not possible to clearly interpret the clay mineral formed in the present study.

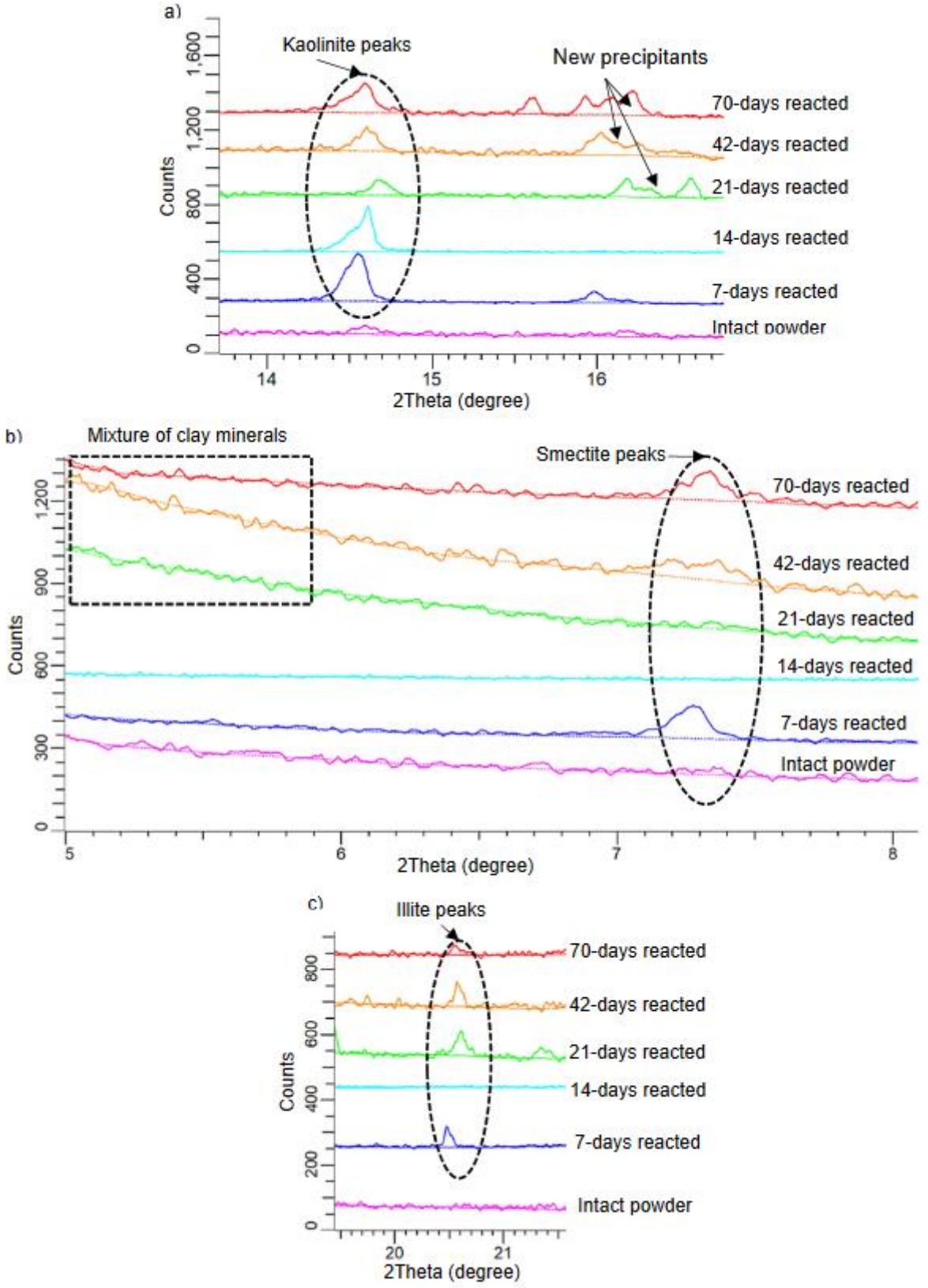

Figure 10. Peaks of secondary precipitants of clay minerals; (a) kaolinite, (b) smectite, and (c) illite identified from XRD analysis.

The formation of silica precipitants was observed in the quartz surface after 70 days reaction in the SEM images shown in Figure 9(h). According to previous studies (Gunnarsson, 2003; Gunnarsson and Arnórsson, 2005; Bhuana et al., 2009; Ngothai et al., 2012), the silica polymerisation mechanism is complex. Generally, the silica polymerisation process can be divided into two processes:

1. Monomeric silica precipitates directly from the solution onto the surfaces and takes place at lower concentrations of dissolved silica. These deposits are dark in colour and have a comparatively high density of about 2.0 g/cc (Bhuana et al., 2009).
2. Silica polymerisation remains as a colloid in the suspension for a long period. This polymerisation occurs due to the rapid nucleation of Si atoms. This nucleation reaction is enhanced by silicic acid. Weres et al. (1982) stated that the subsequent coagulation and flocculation of polymers occur due to the cementation and chemical bonding of Si atoms. The flocculation process continues until the concentration of monomeric silica in the solution reaches the saturation concentration of amorphous silica at that particular fluid temperature. However, this precipitation process is heavily dependent on factors such as temperature, pH value, salt concentration, and residence time (Brown, 2011).

The results of the geochemical modelling show that the negativity of the SI of quartz decreases with time and becomes slightly positive in the final stage of the simulation after 56 days. Hence, the formation of amorphous or monomeric silica can be expected in $scCO_2$/water/granite during long-term reaction. However, the introduction of CO_2 into the system does not influence the dissolution and precipitation kinetics of silica (Lin et al., 2008).

4. Conclusions

Laboratory reactivity tests and geochemical simulations were conducted on a $scCO_2$/water/granite system at 100 °C and 10 MPa in order to characterise the mineral dissolution and precipitation of Harcourt granite during long-term reactions. Based on the results of the experiments and geochemical simulations, the following conclusions are drawn:

- The increase in acidity level of the system due to the dissolution of $scCO_2$ in the water at 100 °C and 10 MPa promotes the dissolution of the mineral phases of Harcourt granite. Hence, mainly alkali (Na and K) and alkali-earth metals (Ca and Mg) are released into the acidic medium. The mineral dissolution process is initially accelerated due to the high H^+ activity in the initial solution. However, the reaction rates decrease with time due to the consumption of H^+ ions from the solution for these chemical reactions.
- Significant dissolution of anorthite takes place even in the initial stages of the reaction period, and albite, annite, and biotite phases also dissolve considerably. Quartz dissolution is slow compared with that of other minerals present in Harcourt granite. Since the solution is under-saturated with anorthite, albite, K-feldspar, and biotite minerals even after 210 days of reaction, the dissolution of these minerals continues during long-term reactivity. Hence, considerable mineral dissolution takes place in the outer periphery of a CO_2-based geothermal reservoir where the reservoir rock is exposed to water in the form of vapour with dissolved $scCO_2$. Mineral surface pitting and the formation of new pore spaces in the rock matrix facilitate smooth fluid flow in geothermal reservoirs.
- Clay minerals form in a $scCO_2$/water/granite system at 100 °C and 10 MPa by consuming the cations from the saturated medium during long-term reactions. The possible precipitants of clay minerals in an acidic medium at 100 °C are identified as kaolinite, smectite, and illite. Importantly, there is a possibility of calcite precipitation during long-term reaction by consuming Ca cations from the saturation medium, and there is therefore the potential for CO_2 storage in the outer periphery of CO_2-based geothermal reservoirs during long-term operation.
- The precipitation of silica as amorphous or monomeric silica is possible in a $scCO_2$/water/granite system at 100 °C and 10 MPa during long-term reaction once the system is over-saturated with dissolved silica.
- However, a reduction in the pore volume of the outer periphery of a geothermal reservoir occurs with time due to the permeant deposition of secondary precipitants. Nevertheless, considerable dissolution takes place in reservoir rock in an acidic medium. Therefore, reservoir permeability is not significantly affected during the long-term operation of enhanced geothermal systems.

However, the creation of a sealing zone in the outermost periphery in a geothermal reservoir is beneficial for the safe operation of the reservoir.

- It is recommended to evaluate the net change in reservoir rock porosity with time using a geochemical model by simulating long-term reactivity in order to clearly identify the extent of mineral dissolution and precipitation and their influence on the permeability properties of geothermal reservoirs.

References

Aagaard P, Helgeson HC (1982). Thermodynamic and kinetic constraints on reaction rates among minerals and aqueous solutions; I, Theoretical considerations. American Journal of Science 282: 237-285.

Alemu BL, Aagaard P, Munz IA, Skurtveit E (2011). Caprock interaction with CO_2: A laboratory study of reactivity of shale with supercritical CO_2 and brine. Applied Geochemistry 26: 1975-1989.

Amrhein C, Suarez DL (1992). Some factors affecting the dissolution kinetics of anorthite at 25 C. Geochimica et Cosmochimica Acta 56: 1815-1826.

Aquilanti V, Mundim KC, Elango M, Kleijn S, Kasai T (2010). Temperature dependence of chemical and biophysical rate

processes: Phenomenological approach to deviations from Arrhenius law. Chemical Physics Letters 498: 209-213.

Bhuana D, Ashman PJ, Nathan G (2009). Silica deposition in Enhanced Geothermal Systems. Proceeding of the Australia Geothermal Conference 2009.

Bischoff JL, Rosenbauer RJ (1996). The alteration of rhyolite in CO_2 charged water at 200 and 350°C: The unreactivity of CO_2 at higher temperature. Geochimica et Cosmochimica Acta 60: 3859-3867.

Boudot JP, Maitat O, Merlet D, Rouiller J (1996). Occurrence of non-monomeric species of aluminium in undersaturated soil and surface waters: consequences for the determination of mineral saturation indices. Journal of Hydrology 177: 47-63.

Brown DW (2000). A hot dry rock geothermal energy concept utilizing supercritical CO_2 instead of water. Proceedings of the twenty-fifth workshop on geothermal reservoir engineering, Stanford University pp. 233-238.

Brown Kevin (2011). Thermodynamics and kinetics of silica scaling. International Workshop on Mineral Scaling, 2011.

Chandrasekharam D, Ranjith PG (2020). CO_2 emissions from renewables: solar pv, hydrothermal and EGS sources. Geomechanics and Geophysics for Geo-Energy and Geo-Resources 6: 13. doi: 10.1007/s40948-019-00135-y

Chen L, Jin X, Chen H, He Z, Qiu et al. (2020). Grain size distribution and clay mineral distinction of rare earth ore through different methods. Minerals 10: 353.

Gales C (1905). About a case of kaolinitisation in granite by a cold CO_2 bearing water. Zenlt. Geol. Min. Palisant.

Golubev SV, Pokrovsky OS, Schott J (2005). Experimental determination of the effect of dissolved CO_2 on the dissolution kinetics of Mg and Ca silicates at 25°C. Chemical Geology 217: 227-238.

Gruber C, Kutuzov I, Ganor J (2016). The combined effect of temperature and pH on albite dissolution rate under far-from-equilibrium conditions. Geochimica et Cosmochimica Acta 186: 154-167.

Gunnarsson I, Arnórsson S (2003). Silica scaling: The main obstacle in efficient use of high-temperature geothermal fluids. Proc. Int. Geotherm. Conf. pp. 24–29.

Gunnarsson I, Arnórsson S (2005). Impact of silica scaling on the efficiency of heat extraction from high-temperature geothermal fluids. Geothermics 34: 320-329.

Hänchen M, Prigiobbe V, Storti G, Seward TM, Mazzotti M (2006). Dissolution kinetics of fosteritic olivine at 90–150°C including effects of the presence of CO_2. Geochimica et Cosmochimica Acta 70: 4403-4416.

Henley RW, Ellis AJ (1983). Geothermal systems ancient and modern: a geochemical review. Earth-science Reviews 19: 1-50.

Hitchon B, Gunter WD, Gentzis T, Bailey RT (1999). Sedimentary basins and greenhouse gases: a serendipitous association. Energy Conversion and Management 40: 825-843.

Isaka BLA, Ranjith PG, Rathnaweera TD (2019). The use of super-critical carbon dioxide as the working fluid in enhanced geothermal systems (EGSs): a review study. Sustainable Energy Technologies and Assessments 36: 100547.

Jayasekara DW, Ranjith PG, Wanniarachchi WAM, Rathnaweera TD, Van Gent D (2020). CO_2-brine-caprock interaction: Reactivity experiments on mudstone caprock of South-west Hub geo-sequestration project. Journal of Petroleum Science and Engineering 107011.

Jung Y, Xu T, Dobson PF, Chang N, Petro M (2014). Experiment-based modeling of geochemical interactions in CO_2-based geothermal systems. 38th Annual Workshop on Geothermal Reservoir Engineering, Stanford, CA, Feb. 11-13, 2013, 2014.

Kalinowski BE, Schweda P (1996). Kinetics of muscovite, phlogopite, and biotite dissolution and alteration at pH 1–4, room temperature. Geochimica et Cosmochimica Acta 60: 367-385.

Kampman N, Bickle M, Becker J, Assayag N, Chapman H (2009). Feldspar dissolution kinetics and Gibbs free energy dependence in a CO_2-enriched groundwater system, Green River, Utah. Earth and Planetary Science Letters 284: 473-488.

Kim CM, Han R, Jeong G, Young J, Jong O (2016). Internal structure and materials of the Yangsan fault, Bogyeongsa area, Pohang, South Korea. Geosciences Journal 20: 759-773.

Köhler SJ, Dufaud FO, Eric H (2003). An experimental study of illite dissolution kinetics as a function of pH from 1.4 to 12.4 and temperature from 5 to 50°C. Geochimica et Cosmochimica Acta 67: 3583-3594.

Krausz K (1974). Potassium-Barium exchange in phlogopite. The Canadian Mineralogist 12: 394-398.

Laidler KJ (1972). Unconventional applications of the Arrhenius law. Journal of Chemical Education 49: 343.

Lasaga AC (1984). Chemical kinetics of water-rock interactions. Journal of Geophysical Research: Solid Earth 89: 4009-4025.

Li MX, Ricard LP, Underschultz J, Freifeld BM (2016). Reducing operational costs of CO_2 sequestration through geothermal energy integration. International Journal of Greenhouse Gas Control 44: 238-248.

Lide DR (2004). CRC handbook of chemistry and physics, CRC press.

Lin H, Fujii T, Takisawa R, Takahashi T, Hashida T (2008). Experimental evaluation of interactions in supercritical CO_2/water/rock minerals system under geologic CO_2 sequestration conditions. Journal of Materials Science Letters 43: 2307-2315.

Liu L, Suto Y, Bignall G, Yamasaki N, Hashida T (2003). CO_2 injection to granite and sandstone in experimental rock/hot water systems. Energy Conversion and Management 44: 1399-1410.

Lo RC, Kaszuba J, Moore J, McPherson B (2012). Supercritical CO_2 in a granite-hosted geothermal system: Experimental insights into multiphase fluid-rock interactions. Proceedings of the Thirty-Seventh Workshop on Geothermal Reservoir Engineering, Stanford University, 2012.

Na J, Xu T, Yuan Y, Feng B, Tian H et al. (2015). An integrated study of fluid–rock interaction in a CO_2-based enhanced geothermal system: A case study of Songliao Basin, China. Applied Geochemistry 59: 166-177.

Ngothai Y, Lane D, Kuncoro G, Yanagisawa N, Rose P et al. (2012). Effect of geothermal brine properties on silica scaling in enhanced geothermal systems. Geothermal Resources Council Annual Meeting 2012-Geothermal: Reliable, Renewable, Global, GRC 2012.

Oelkers EH, Schott J (1995). Experimental study of anorthite dissolution and the relative mechanism of feldspar hydrolysis. Geochimica et Cosmochimica Acta 59: 5039-5053.

Palandri JL, Kharaka YK (2004). A compilation of rate parameters of water-mineral interaction kinetics for application to geochemical modeling. Geological Survey Menlo Park CA.

Pan F, McPherson BJ, Kaszuba J (2017). Evaluation of CO_2-fluid-rock interaction in enhanced geothermal systems: field-scale geochemical simulations. Geofluids.

Parkhurst DL (1995). User's guide to PHREEQC: A computer program for speciation, reaction-path, advective-transport, and inverse geochemical calculations, US Department of the Interior, US Geological Survey.

Pereira JSF, Knorr CL, Pereira LSF, Moraes DP, Paniz JNG et al. (2011). Evaluation of sample preparation methods for polymer digestion and trace elements determination by ICPMS and ICPOES. Journal of Analytical Atomic Spectrometry 26: 1849-1857.

Petro M (2013). Experimental study of rock-fluid interaction using automated multichannel system operated under conditions of CO_2-based geothermal systems.

Randolph JB, Saar MO (2011). Coupling carbon dioxide sequestration with geothermal energy capture in naturally permeable, porous geologic formations: Implications for CO_2 sequestration. Energy Procedia 4: 2206-2213.

Ré CL, Kaszuba JP, Moore JN, McPherson BJ (2014). Fluid–rock interactions in CO_2-saturated, granite-hosted geothermal systems: Implications for natural and engineered systems from geochemical experiments and models. Geochimica et Cosmochimica Acta 141: 160-178.

Remoroza AI, Moghtaderi B, Doroodchi E (2015). Fluid-Rock interaction under reservoir conditions pertinent to hot dry rock-engineered geothermal systems. Proceedings World Geothermal Congress, pp. 19-25.

Shvartsev S (2013). Water-rock interaction: implications for the origin and program of global evolution. International Journal of Sciences.

Singh M, Tangirala SK, Chaudhuri A (2020). Potential of CO2 based geothermal energy extraction from hot sedimentary and dry rock reservoirs, and enabling carbon geo-sequestration. Geomechanics and Geophysics for Geo-Energy and Geo-Resources 6: 16.

Span R, Wagner W (1996). A new equation of state for carbon dioxide covering the fluid region from the triple-point temperature to 1100 K at pressures up to 800 MPa. Journal of Physical and Chemical Reference Data, 25, 1509-1596.

Sugama T, Ecker L, Butcher T (2010). Carbonation of Rock Minerals by Supercritical Carbon Dioxide at 250°C. Brookhaven National Laborotory (BNL).

Sugama T, Gill S, Ecker L, Butcher T, Warren J (2011). Susceptibility of Granite Rock to $ScCO_2$/Water at 200°C and 250°C. Brookhaven National Laboratory (BNL).

Suto Y, Liu L, Yamasaki N, Hashida T (2007). Initial behavior of granite in response to injection of CO2-saturated fluid. Applied Geochemistry 22: 202-218.

Suto Y, Yamasaki Y, Hashida T, Yamasaki N (2000). Effects of CO2 on Water/Rock Chemical Interactions in Geothermal Reservoir Environment. Proc. World Geothermal Congress, 3901-3906.

Turgay SO, Yaşar E (2021). Evaluation of hydrocarbon occurrences of Hatay with integrated methods, SE Turkey. Geomechanics and Geophysics for Geo-Energy and Geo-Resources 7: 54.

Ueda A, Kato K, Ohsumi T, Yajima T, Ito H et al. (2005). Experimental studies of CO2-rock interaction at elevated temperatures under hydrothermal conditions. Geochemical Journal 39: 417-425.

Ueda, Akira, Ajima, Shuji & Yamamoto, Masahiro 2001. Isotopic study of carbonate minerals from the Sumikawa geothermal area and its application to water movement. Journal of the Geothermal Research Society of Japan, 23, 181-196.

Weres, Oleh, Yee, Andrew & Tsao, Leon 1982. Equations and type curves for predicting the polymerization of amorphous silica in geothermal brines. Society of Petroleum Engineers Journal, 22, 9-16.

Xu T (2012). Mineral carbonation in a CO2-EGS geothermal reservoir. Matrix 6-7.

Xu T, Feng G, Shi Y (2014). On fluid–rock chemical interaction in CO_2-based geothermal systems. Journal of Geochemical Exploration 144: 179-193.

Xu T, Pruess K, Apps J (2008). Numerical studies of fluid-rock interactions in enhanced geothermal systems (EGS) with CO_2 as working fluid.

Xu T, Senger R, Finsterle S (2011). Bentonite alteration due to thermal-hydro-chemical processes during the early thermal period in a nuclear waste repository. Nuclear Technology 174: 438-451.